Available online at www.sciencedirect.com
ScienceDirect
Advances in Space Research 41 (2008) 1733–1743
ADVANCES IN SPACE RESEARCH (a COSPAR publication)
www.elsevier.com/locate/asr

Fractal signatures for multiscale processing of hyperspectral image data

Pinliang Dong

Department of Geography, University of North Texas, P.O. Box 305279, Denton, TX 76203, USA

Received 31 October 2006; received in revised form 28 March 2007; accepted 30 April 2007

Abstract

A multiscale approach to hyperspectral image data analysis using fractal signatures was proposed and implemented in the Interactive Data Language (IDL). For 2-D hyperspectral curves, fractal signature measures the changes in curve length with changing scale. Using NASA's Earth Observing-1 (EO-1) Hyperion image from a study area near Denton, Texas, USA, the capabilities of fractal signatures in discriminating different land cover types were presented in three different ways: (1) fractal signature curves, (2) distances between fractal signatures, and (3) fractal signature images. The asymmetry in length measurement was found to be effective in handling hyperspectral curves obtained from Hyperion radiance data. The contribution of fractal signature images was shown through comparison of image classification results. The results from the Hyperion radiance data suggest that fractal signatures at certain scales can reveal important differences in land cover types.

Keywords: Fractal signature; Multiscale; Hyperspectral; Hyperion; Land cover

1. Introduction

1.1. Image analysis in scale-space

Multispectral data can be represented in three principal ways: image space, spectral space, and feature space (Landgrebe, 1997). In image space, pixels are arranged in geometric relationship to one another. In spectral space, variations within pixels are expressed as a function of spectral wavelength. In feature space, pixels are displayed as points in an N-dimensional space. With more and more remotely sensed data being acquired by airborne and spaceborne platforms, a key issue in image analysis is how to extract information from data more effectively and efficiently. Many information extraction methods for hyperspectral data have been developed (for example, Landgrebe, 1997; Tsai and Philpot, 1998; Hsu and Tseng, 1999, 2000; Schowengerdt, 2006). In addition to the three data representation methods, multiscale representation is also important because many natural objects appear in different ways depending on the scale of observation. The scale-space concept has attracted increased interest in signal processing and numerical analysis. For example, as a type of multiscale representation, wavelet transform has been used for hyperspectral image data analysis in various applications (Hsu and Tseng, 2000; Mathur et al., 2002; Kaewpijit et al., 2003; Pu and Gong, 2004). An important requirement in multiscale representation is that structures at coarse scales should constitute simplifications of corresponding structures at finer scales (Lindeberg, 1994a,b). In other words, structures at coarse scales are not simply a smoothed version of the structures at finer scales.

1.2. Fractal geometry for analysis of remotely sensed images

Many natural objects are so complex and irregular that models of classical geometry are sometimes insufficient to describe them. Mandelbrot (1977) described these objects using the term fractal, after the Latin fractus which means broken or irregular fragments. Fractals can be generally

E-mail address: pdong@unt.edu

0273-1177/$34.00
doi:10.1016/j.asr.2007.04.090

defined as geometric shapes that have two properties: self-similarity and fractional dimensionality (Devaney, 1990). Fractal geometry has received increased attention as a novel model for natural phenomena since Mandelbrot's work (Mandelbrot, 1977, 1983). In the areas of remote sensing applications, a number of studies have been carried out to evaluate the usefulness of fractals for analysis of land surface images. De Cola (1989) used fractal analysis of perimeters and areas derived from a classified Landsat TM image to study the complexity of land cover types, and concluded that it is possible to associate land cover patterns with fractal measurements. Lam (1990) analysed the fractal dimensions of different Landsat TM images and bands, which shows that different land types have different levels of fractal dimensions in different bands. Rees (1992) measured fractal dimensions of ice-sheet surfaces using Landsat data. Roach and Fung (1994) analysed the fractal scaling characteristics of spectrally classified Landsat TM images in a logging area in southern British Columbia, Canada, and concluded that fractal geometry is not useful as a primary classification tool, but fractal geometry can be a useful tool for investigating and quantifying the complicated and intimate relationship between forests and their underlying surface topography. Qiu et al. (1999) computed the fractal dimensions for each of the 224 spectral bands from two AVIRIS scenes selected from a rural area and an urban area in Los Angeles, California, and concluded that fractal dimension could be used to distinguish landscape types and for screening noisy bands.

All the above examples of fractals for remote sensing application put emphasis on estimation of fractal dimension over an entire image or large image patches and can be viewed as "global fractal analysis" of the images. In many applications, a remotely sensed image is supposed to contain different spatial and spectral patterns and therefore a "local fractal analysis" seems to be more desirable. Dellepiane et al. (1991) used a modified version of the "blanket method" proposed by Peleg et al. (1984) for estimation of the fractal dimension for pixel windows in a Seasat SAR image. The fractal dimension image is then combined with intensity and texture features for recognition of land cover types. De Jong and Burrough (1995) used a triangular prism surface area method (TPSAM) proposed by Clarke (1986) to assess local fractal dimensions of remotely sensed images for classification of Mediterranean vegetation types using Landsat TM airborne Geophysical Environmental Research (GER) Imaging Spectrometer images. Based on the analysis of fractal dimension values resulted from the variogram method and the triangular prism surface area method for calculation of fractal dimension, they concluded that remotely sensed images of the land cover units are not true fractals. The finding is consistent with the conclusions of Burrough (1989) which indicate that the landscape surfaces are not true fractals. They also concluded that local dimension is insufficient for the automatic classification of TM imagery into land cover categories, though local dimension seems to reflect the different vegetation types in the study area. These studies suggest that fractal dimension has limitations in image analysis. Such limitations are also discussed in Dong (2000a,b) and Myint (2003). In fact, an image intensity surface may only be fractal in a limited scale range, but may not be fractal for the entire scale range (Pentland, 1984; Peleg et al., 1984). Beyond the proper scale range, it is theoretically inappropriate to calculate fractal dimension for an image that is not fractal, even though the so-called fractal dimensions might be useful descriptors for image analysis in some cases. Therefore, new measures that work for both fractals and non-fractals would be a better choice than fractal dimension for image analysis.

1.3. Objectives of this study

It is generally believed that the shape of a reflectance spectrum can usually be broken down into two components: the general shape of the spectrum and the distinctive absorption features in the spectrum. Many pure materials, such as minerals, can be recognized by the position, strength and shape of their absorption features, whereas many other materials, such as soils and rocks, may lack distinctive absorption features. This paper presents a multiscale method that characterises spectra derived from hyperspectral images using fractal signatures. Fractal signature was first introduced by Peleg et al. (1984) to characterise image textures. It measures the change in the area of an image intensity surface with changing scale, and can be used as a multiscale measure for both fractals and non-fractals (Peleg et al., 1984). The method was applied to NASA's Earth Observing-1 (EO-1) Hyperion data from a study area in North Texas, USA to aid in land cover mapping. However, this study does not deal with textures of image intensity surfaces. Rather it focuses on individual spectrum derived from each pixel location in a hyperspectral image. The effectiveness of fractal signatures in discriminating different land cover types is illustrated using (1) fractal signature curves, (2) distances between fractal signatures, and (3) fractal signature images and classifications.

2. Study area and data

The study area is located in the Ray Roberts Greenbelt near Denton, Texas, USA (Fig. 1). The area is relatively flat and has an average elevation of about 163 m. In this study, land cover types are divided into five general categories: (1) dense canopy vegetation (bottomland forest and upland forest), (2) sparse canopy vegetation (rangeland, shrub land, and agricultural land), (3) bare soil, (4) urban, and (5) water.

The hyperspectral image data were acquired by NASA's Earth Observing-1 (EO-1) Hyperion on August 30, 2004. The launch of the EO-1 platform in November

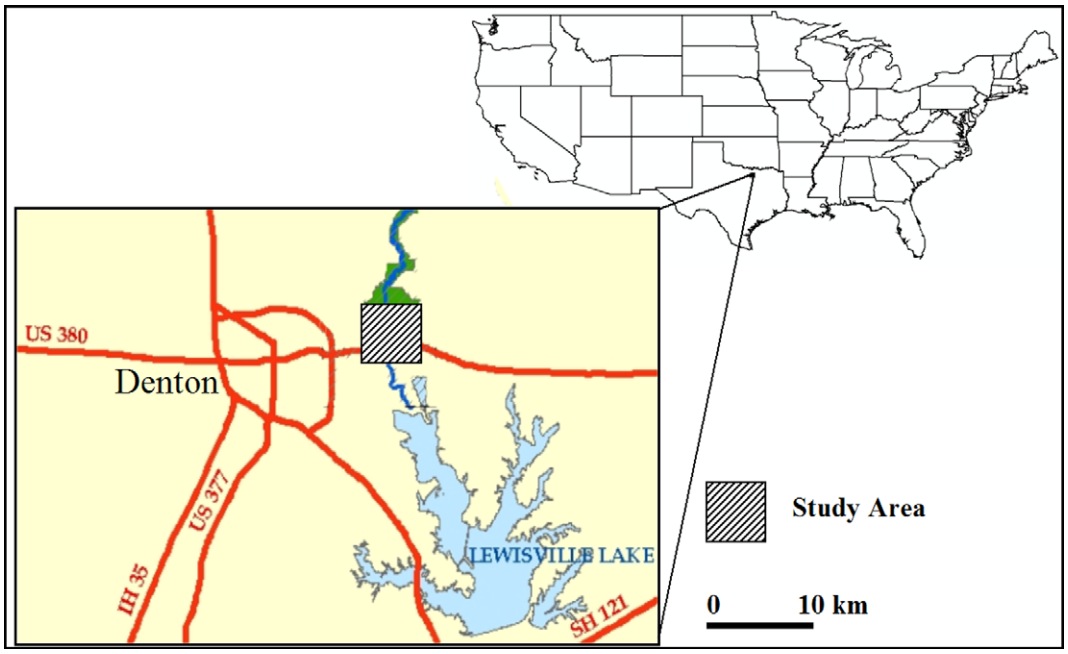

Fig. 1. Location of the study area.

2000 marks the first operational test of NASA's "New Millennium" spaceborne hyperspectral technology for Earth observation (NASA, 2002). The theme of the EO-1 mission is the evaluation of advanced earth observation instruments through a combination of direct measurements of performance and a broad range of application studies (Ungar et al., 2003). The Hyperion imaging spectrometer onboard the EO-1 is the first high spatial resolution imaging spectrometer to orbit the Earth. More information on the EO-1 and Hyperion can be found in Pearlman et al. (2003) and Ungar et al. (2003). The processing level for the 242-band (from 400 to 2500 nm) Hyperion data was 1R (radiometrically corrected). The full dataset has 256 pixels and 6702 lines with a pixel size of 30 m. The original 242 bands were reduced to 138 bands, by excluding the bands with (1) all pixels being zeros, (2) low signal to noise ratio at both spectral ends (<430 nm and >2400 nm), (3) overlap of the two spectrometers (VNIR and SWIR), and (4) strong atmospheric water absorption. Fig. 2 is a sub-image of 182 by 182 pixels (5.46 km by 5.46 km) in the study area. The numbers 1–10 on the image show the approximate pixel locations where spectral curves were extracted for selected land cover types. Numbers 1 and 2 are for dense canopy vegetation, 3 and 4 for sparse canopy vegetation, 5 and 6 for soil, 7 and 8 for water (Lake Lewisville), and 9 and 10 for urban areas. The spectral curves for the selected land cover types are shown in Fig. 3. It should be noted that the band numbers in Fig. 3 are for the reduced set of 138 bands, not corresponding to the original 242 Hyperion bands. These band numbers should be interpreted as indices rather than actual wavelengths.

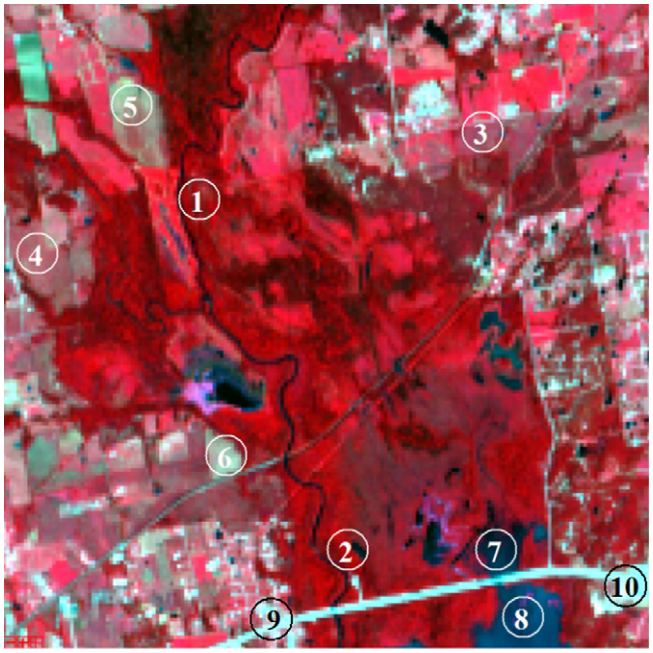

Fig. 2. EO-1 Hyperion image of the study area in the Ray Roberts Greenbelt near Denton, Texas, USA. The numbers show the approximate pixel locations where spectral curves were extracted. Image size: 182 by 182 pixels (5.46 km by 5.46 km).

3. Methodology

Peleg et al. (1984) defined fractal signature as the change in measured area with changing scale when studying texture analysis and classification of digital images. Their study was based on 3-D image intensity surfaces (i.e., pixel locations in the x–y plane and pixel values in the z direc-

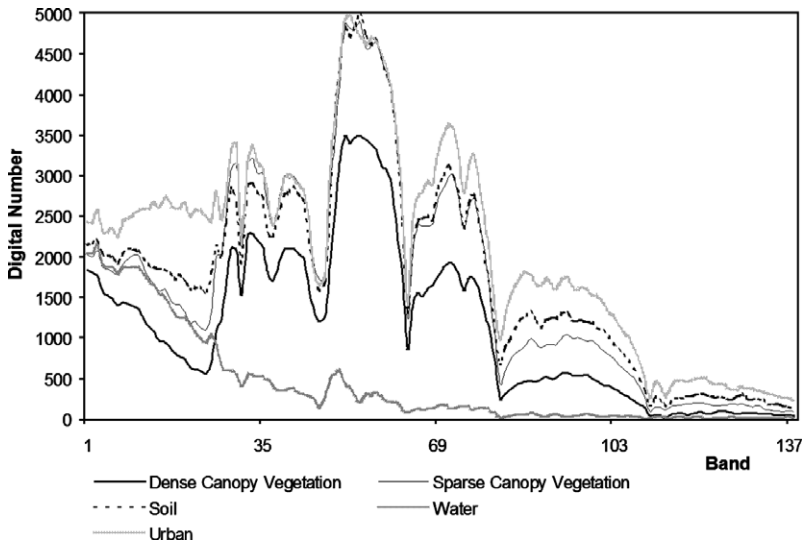

Fig. 3. Spectral curves of selected land cover types derived from locations in Fig. 2.

tion), whereas this study is based on 2-D profiles (i.e., hyperspectral band numbers in the x direction and pixel values in the y direction). Unlike texture analysis where a pixel and its neighbors are taken into account and the output is a texture feature image with degraded spatial resolution, analysis of hyperspectral profiles deals with the pixel values in hyperspectral bands at individual pixel locations. Therefore, the output image will have the same spatial resolution as the input hyperspectral image. A 2-D profile can be considered a special case of a 3-D surface. A 3-D surface has surface area while a 2-D profile has profile length. As a general introduction of the methodology, the following description is based on 3-D surfaces. Most of the notations and formalism are adopted from Peleg et al. (1984).

Given an image gray level function $g(i,j)$, the surface of $g(i,j)$ can be covered with a "blanket" of thickness 2ε ($\varepsilon = 1,2,\ldots,n$), where ε is used as the measurement scale. The covering blanket is defined by its upper surface (u_ε) and lower surface (b_ε). Setting $u_0(i,j) = b_0(i,j) = g(i,j)$, the upper surfaces and lower surfaces can be constructed using the following expressions:

$$u_\varepsilon(i,j) = \max\left\{u_{\varepsilon-1}(i,j)+1, \max_{|(m,n)-(i,j)\leqslant 1|} u_{\varepsilon-1}(m,n)\right\} \quad (1)$$

$$b_\varepsilon(i,j) = \min\left\{b_{\varepsilon-1}(i,j)-1, \min_{|(m,n)-(i,j)\leqslant 1|} b_{\varepsilon-1}(m,n)\right\} \quad (2)$$

where (m,n) is an immediate neighbor of (i,j). Eq. (1) ensures that the new upper surface u_ε is higher by at least 1 from $u_{\varepsilon-1}$. Similarly, Eq. (2) ensures that the new lower surface b_ε is lower by at least 1 from $b_{\varepsilon-1}$. Fig. 4 illustrates an original surface and its upper and lower surfaces at $\varepsilon = 1$ and 2.

The volume of the blanket is calculated using

$$v_\varepsilon = \sum_{i,j}(u_\varepsilon(i,j) - b_\varepsilon(i,j)) \quad (3)$$

and the surface area of the blanket is defined as

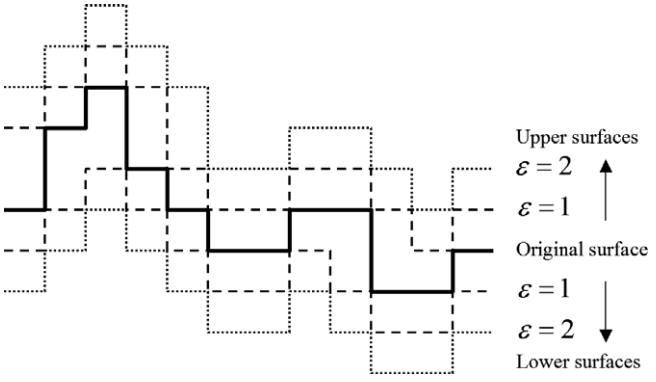

Fig. 4. An original surface and its upper and lower surfaces at $\varepsilon = 1,2$.

$$A(\varepsilon) = \frac{(v_\varepsilon - v_{\varepsilon-1})}{2} \quad (4)$$

According to Mandelbrot (1983), the area of a fractal surface can be expressed as

$$A(\varepsilon) = F\varepsilon^{2-D} \quad (5)$$

where F is a constant, and D is the "fractal dimension". For measurement of both fractal and non-fractal surfaces, fractal signature $S(\varepsilon)$ is computed for each ε ($\varepsilon = 2,3,4,\ldots,n$) by finding the slope of the best fitting straight line through the three points

$$(\log(\varepsilon-1), \log(A(\varepsilon-1))), \quad (\log(\varepsilon), \log(A(\varepsilon))),$$
$$(\log(\varepsilon+1), \log(A(\varepsilon+1)))$$

Suppose p and q are two spectra derived from two different land cover types, the difference between the two fractal signatures S_p and S_q is measured by the distance $D(p,q)$

$$D(p,q) = \sum_\varepsilon \left\{\left[(S_p(\varepsilon) - S_q(\varepsilon))^2\right] \cdot \log\left(\frac{\varepsilon+\frac{1}{2}}{\varepsilon-\frac{1}{2}}\right)\right\} \quad (6)$$

In his paper "How long is the coast of Great Britain: statistical self-similarity and fractional dimension", Mandelbrot (1967) noticed the asymmetry in length measurement: reversing the role of land and water, different coastline lengths might result. To make use of this asymmetry, Peleg et al. (1984) divided the above surface area measurements into two parts: measuring the area of the gray level surface from "above" and measuring the area of the surface from "below." Therefore, the volume definition of Eq. (3) can be changed to the following two definitions of "upper volume" v_ε^+ and "lower volume" v_ε^-:

$$v_\varepsilon^+ = \sum_{i,j}(u_\varepsilon(i,j) - g(i,j)) \tag{7}$$

$$v_\varepsilon^- = \sum_{i,j}(g(i,j) - b_\varepsilon(i,j)) \tag{8}$$

Accordingly, "top area" $A^+(\varepsilon)$ and "bottom area" $A^-(\varepsilon)$ are defined as

$$\begin{aligned} A^+(\varepsilon) &= v_\varepsilon^+ - v_{\varepsilon-1}^+ \\ &= \sum_{i,j}(u_\varepsilon(i,j) - g(i,j)) - \sum_{i,j}(u_{\varepsilon-1}(i,j) - g(i,j)) \\ &= \sum_{i,j}(u_\varepsilon(i,j) - u_{\varepsilon-1}(i,j)) \end{aligned} \tag{9}$$

$$\begin{aligned} A^-(\varepsilon) &= v_\varepsilon^- - v_{\varepsilon-1}^- \\ &= \sum_{i,j}(g(i,j) - b_\varepsilon(i,j)) - \sum_{i,j}(g(i,j) - b_{\varepsilon-1}(i,j)) \\ &= \sum_{i,j}(b_{\varepsilon-1}(i,j) - b_\varepsilon(i,j)) \end{aligned} \tag{10}$$

Taking into account the asymmetry between fractal signatures of upper surfaces and lower surfaces, the distance between two fractal signatures S_p and S_q is defined as

$$\begin{aligned} D(p,q) = \sum_\varepsilon \Bigg\{ &\left[(S_p^+(\varepsilon) - S_q^+(\varepsilon))^2 + (S_p^-(\varepsilon) - S_q^-(\varepsilon))^2\right] \\ &\cdot \log\left(\frac{\varepsilon + \frac{1}{2}}{\varepsilon - \frac{1}{2}}\right)\Bigg\} \end{aligned} \tag{11}$$

where S^+ and S^- are the fractal signature of the upper surfaces and lower surfaces, respectively. For 2-D hyperspectral curves, the above definitions for volume and surface area become the definitions for area and profile length. Therefore, "upper/lower surfaces" will be replaced by "upper/lower profiles" for 2-D hyperspectral curves in the following discussion. Of particular interest is that "fractal signature images" can be extracted from upper profiles or lower profiles at certain scales (i.e., certain ε values). For example, the differences (distances) between the hyperspectral fractal signatures of the two land cover class samples p and q at each scale ε ($\varepsilon = 2,3,4,\ldots,n$) can be calculated as

$$d_{pq}^+(\varepsilon) = (S_p^+(\varepsilon) - S_q^+(\varepsilon))^2 \tag{12}$$

$$d_{pq}^-(\varepsilon) = (S_p^-(\varepsilon) - S_q^-(\varepsilon))^2 \tag{13}$$

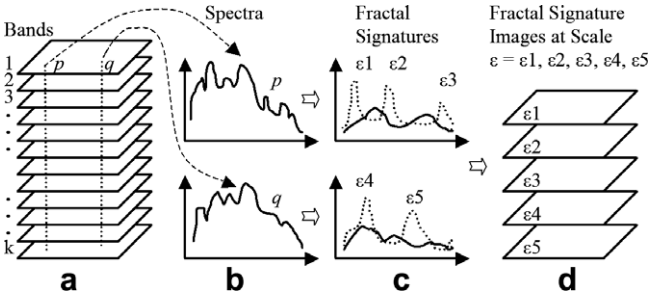

Fig. 5. Creation of fractal signature images.

With the change of scale ε ($\varepsilon = 2,3,4,\ldots,n$), each of the above equations (Eqs. (12) and (13)) generates a distance list of $n-1$ elements. If each list is sorted and the top r ($r < n-1$) distances selected, there will be a total of $2r$ scales (ε values) that can be used for creating fractal signature images. Duplicate ε values in the list of $2r$ elements should be removed to obtain a distinct list of ε values.

From the above description, the process of creating fractal signature images can be summarized as the following:

(1) Spectral curves at sampling locations ($p, q, \ldots$) for different land cover types are retrieved from Hyperspectral image data (Fig. 5a and b).
(2) Fractal signatures are calculated for the sampling spectral curves at multiple scales (Fig. 5c).
(3) Based on the differences in the fractal signatures, a unique list of scales is selected.
(4) For each pixel location in the input hyperspectral image, a spectral curve is retrieved and the fractal signatures of the curve calculated for each selected scale, resulting in fractal signature images at multiple scales (Fig. 5d).

Computer programs were developed using the Interactive Data Language (IDL) in an ENVI™ image processing system for multiscale processing of hyperspectral image data based on fractal signatures. To assess the contribution of fractal signature images, two sets of images are classified using maximum likelihood classification: (1) principal component images derived from the 138-band EO-1 Hyperion image; and (2) principal component images used in (1) plus fractal signature images. The results are presented in the next section.

4. Results and discussion

4.1. Fractal signature curves

Figs. 6–13 are the fractal signature curves with scale $\varepsilon = 2,3,4,\ldots,39$ for both upper and lower profiles of the hyperspectral curves derived from the eight locations shown in Fig. 2. It can be seen that the fractal signatures

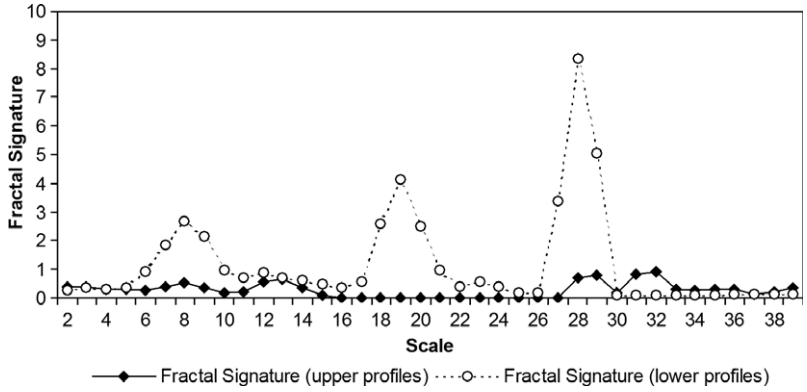

Fig. 6. Fractal signature curves with scale $\varepsilon = 2, 3, 4, \ldots, 39$ (for dense canopy vegetation sample 1).

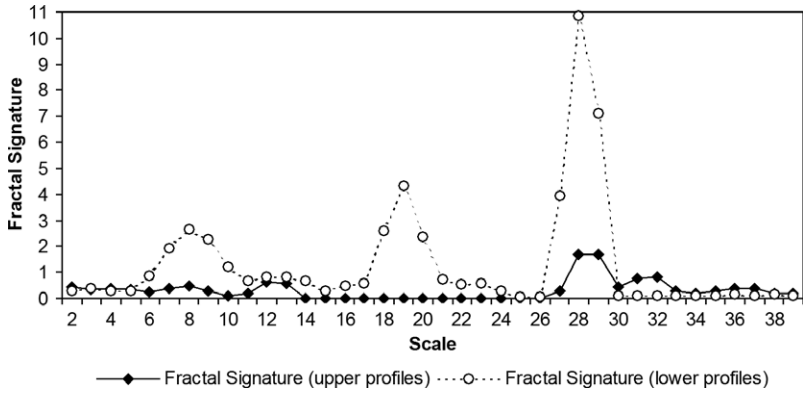

Fig. 7. Fractal signature curves with scale $\varepsilon = 2, 3, 4, \ldots, 39$ (for dense canopy vegetation sample 2).

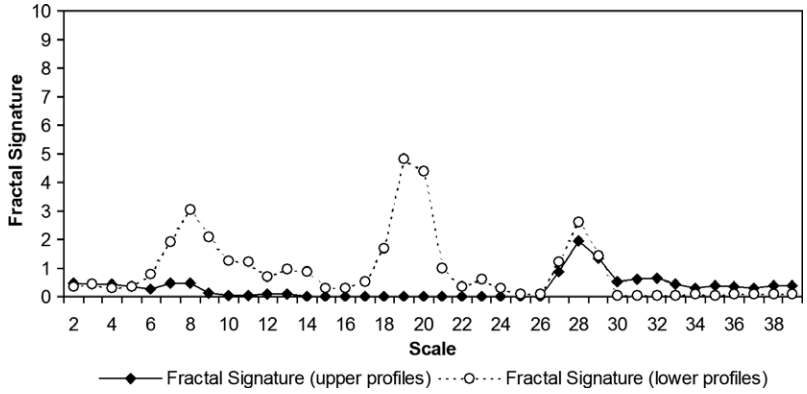

Fig. 8. Fractal signature curves with scale $\varepsilon = 2, 3, 4, \ldots, 39$ (for sparse canopy vegetation sample 1).

from upper profiles are very similar, especially for dense canopy vegetation, sparse canopy vegetation, and soil curves. However, the fractal signatures from lower profiles are quite different. Dense canopy vegetation has obvious peaks in the fractal signatures of the lower profiles at $\varepsilon = 8$, 19, and 28. Sparse canopy vegetation also has obvious peaks at the same locations as dense canopy vegetation, but the amplitude at $\varepsilon = 28$ is much smaller than that shown on the dense canopy vegetation curve. Soils do not show any obvious peak after $\varepsilon = 14$, while lower profile fractal signature curves for water have two obvious peaks between $\varepsilon = 27$ and $\varepsilon = 30$.

4.2. Distances between fractal signatures

Distances between the fractal signatures are calculated using Eq. (6) for the upper profiles (Table 1) and lower profiles (Table 2), respectively. Table 1 and Table 2 also confirm the observation from the fractal signatures: the four different land cover types (dense canopy vegetation, sparse canopy vegetation, soil, and water) in the study area cannot be separated from the upper profile fractal signatures of their spectral curves, but they can be well separated from the lower profile fractal signatures.

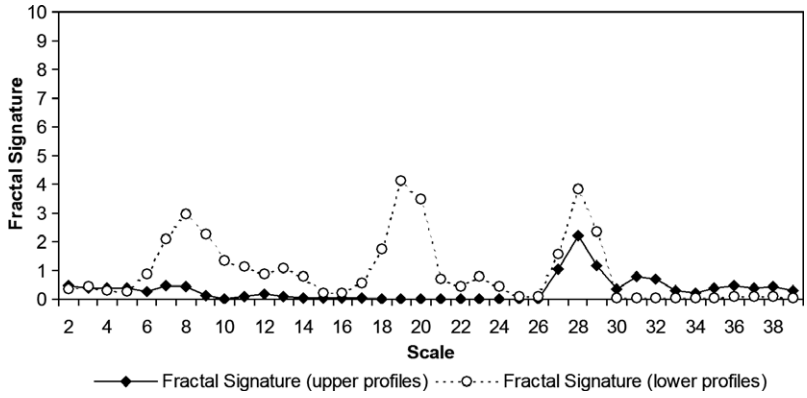

Fig. 9. Fractal signature curves with scale $\varepsilon = 2, 3, 4, \ldots, 39$ (for sparse canopy vegetation sample 2).

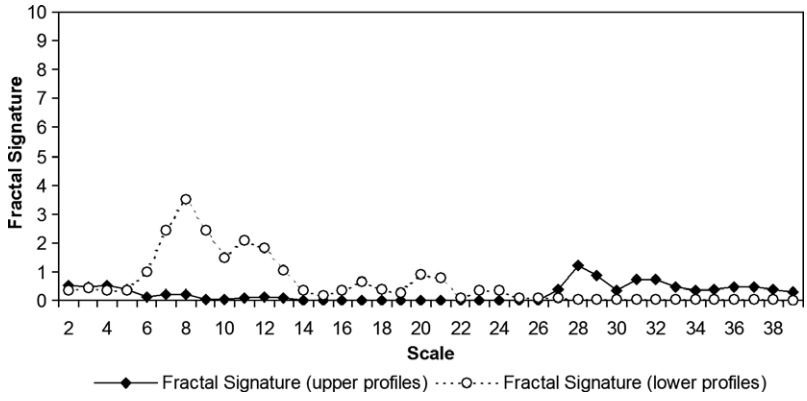

Fig. 10. Fractal signature curves with scale $\varepsilon = 2, 3, 4, \ldots, 39$ (for soil sample 1).

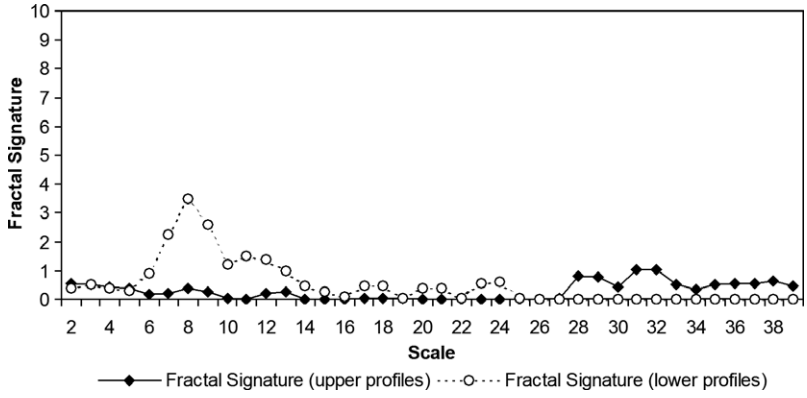

Fig. 11. Fractal signature curves with scale $\varepsilon = 2, 3, 4, \ldots, 39$ (for soil sample 2).

4.3. Fractal signature images

Fig. 14 shows several lower profile fractal signature images obtained from the Hyperion image in Fig. 2 using (a) $\varepsilon = 8$, (b) $\varepsilon = 19$, (c) $\varepsilon = 20$, and (d) $\varepsilon = 28$. Preliminary analyses indicate that the fractal signature images can reflect the land cover types. For example, soils have relatively brighter tones in Fig. 14a, which is in accord with the results from Figs. 6–13 where soils have relatively higher fractal signature values at $\varepsilon = 8$ (for lower profiles). According to Figs. 6–13, lower profile fractal signatures for sparse canopy vegetation have brighter tones than other three features at $\varepsilon = 19$ and 20, as shown in Fig. 14b and 14c. Subtle changes in image tones are also visible when ε changes from 19 (Fig. 14b) to 20 (Fig. 14c). Fig. 14d shows dense canopy vegetation with bright tones and sparse canopy vegetation with less bright tones, which also conforms to the results in Figs. 6–9 at $\varepsilon = 28$. It is also noticed that some noise stripes in the Hyperion data are visible in Fig. 14.

To evaluate the contribution of the fractal signature images for discriminating different land cover types, two sets of images are classified using the maximum likelihood classification: (1) six principal components (PC1, PC2, PC3, PC4, PC6, and PC7) derived from the 138-band Hyperion image; and (2) the six principal component

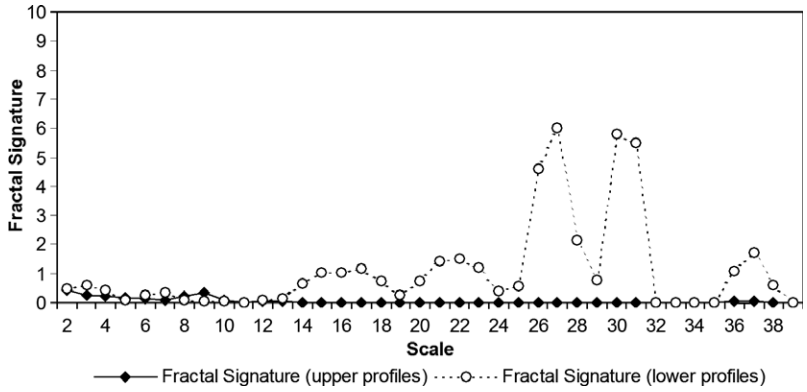

Fig. 12. Fractal signature curves with scale $\varepsilon = 2, 3, 4, \ldots, 39$ (for water sample 1).

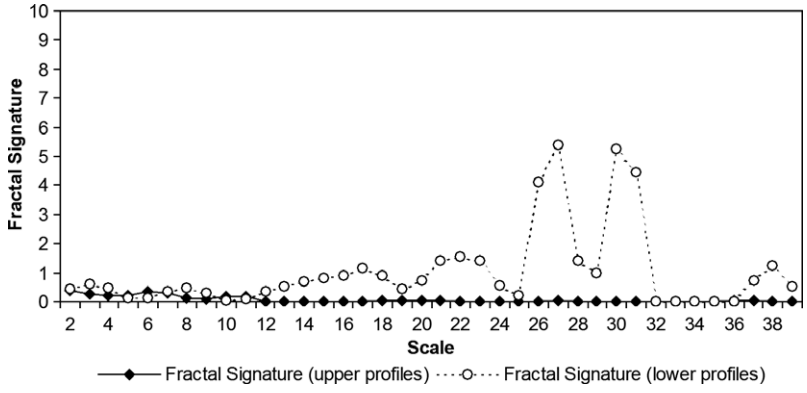

Fig. 13. Fractal signature curves with scale $\varepsilon = 2, 3, 4, \ldots, 39$ (for water sample 2).

Table 1
Distances between upper profile fractal signatures from the eight sampling locations shown in Fig. 2

	DV1	DV2	SV1	SV2	SO1	SO2	WT1	WT2
DV1	0	0.0157	0.0209	0.0092	0.0438	0.0712	0.2304	0.1886
DV2	0.0157	0	0.0296	0.0184	0.0302	0.0527	0.2076	0.1595
SV1	0.0209	0.0296	0	0.0130	0.0239	0.0539	0.2145	0.1753
SV2	0.0092	0.0184	0.0130	0	0.0177	0.0388	0.1801	0.1492
SO1	0.0438	0.0302	0.0239	0.0177	0	0.0162	0.1283	0.0963
SO2	0.0712	0.0527	0.0539	0.0388	0.0162	0	0.1469	0.1283
WT1	0.2304	0.2076	0.2145	0.1801	0.1283	0.1469	0	0.0781
WT2	0.1886	0.1595	0.1753	0.1492	0.0963	0.1283	0.0781	0

DV, dense vegetation; SV, sparse vegetation; SO, soil; WT, water.

Table 2
Distances between lower profile fractal signatures from the eight sampling locations shown in Fig. 2

	DV1	DV2	SV1	SV2	SO1	SO2	WT1	WT2
DV1	0	0.0437	0.6509	0.9895	2.9462	3.0471	5.1283	4.3675
DV2	0.0437	0	0.4352	0.6901	2.4313	2.5192	4.6802	3.9118
SV1	0.6509	0.4352	0	0.1449	0.8852	0.9285	3.1315	2.4785
SV2	0.9895	0.6901	0.1449	0	0.7137	0.8126	3.2571	2.6049
SO1	2.9462	2.4313	0.8852	0.7137	0	0.0572	2.6524	2.0931
SO2	3.0471	2.5192	0.9285	0.8126	0.0572	0	2.5328	1.9656
WT1	5.1283	4.6802	3.1315	3.2571	2.6524	2.5328	0	0.0983
WT2	4.3675	3.9118	2.4785	2.6049	2.0931	1.9656	0.0983	0

DV, dense vegetation; SV, sparse vegetation; SO, soil; WT, water.

images in (1) plus the four fractal signature images in Fig. 14. The classification results are shown in Fig. 15. The overall classification accuracy increased from 64.07% of the first image set to 83.85% of the second image set.

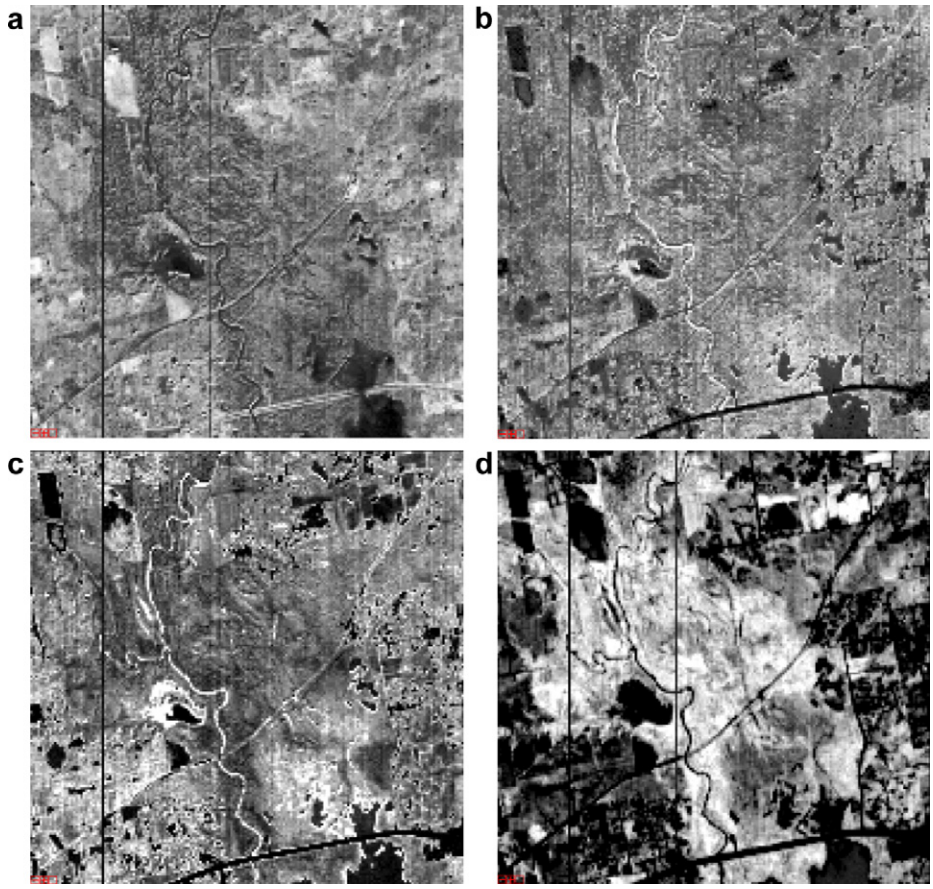

Fig. 14. Lower profile fractal signature images obtained from the Hyperion image in Fig. 2 using (a) $\varepsilon = 8$, (b) $\varepsilon = 19$, (c) $\varepsilon = 20$, and (d) $\varepsilon = 28$.

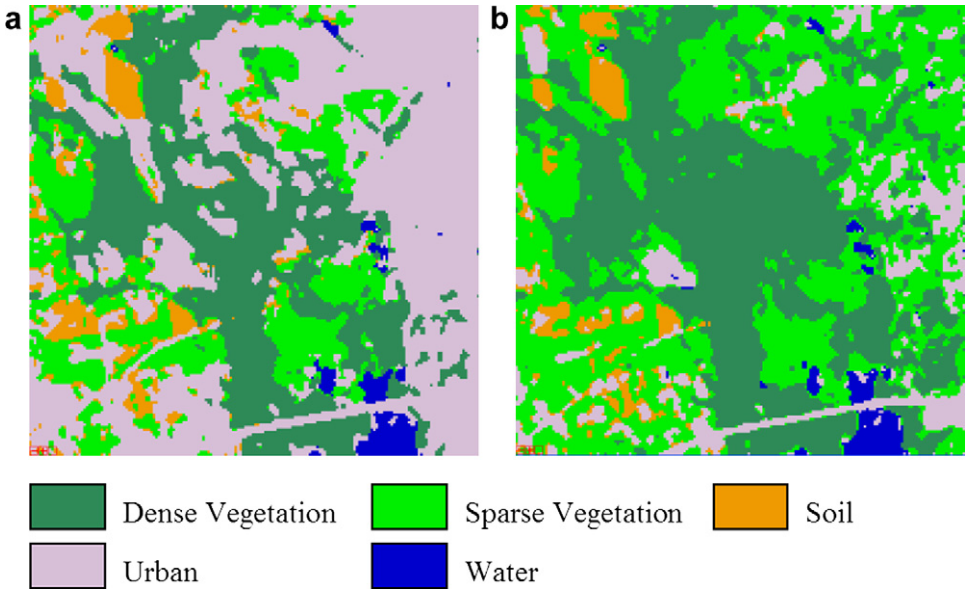

Fig. 15. Maximum likelihood classification results from: (a) six principal components (PC1, PC2, PC3, PC4, PC6, and PC7) derived from the 138-band Hyperion image; and (b) the six principal component images plus the four fractal signature images in Fig. 14.

4.4. Discussion

After examining the results from dense canopy vegetation, sparse canopy vegetation, and soil in 4.1 and 4.2, one would ask: why do fractal signatures from upper profiles look very similar, whereas fractal signatures from lower profiles behave differently? This can be explained by the profile construction process as expressed in Eq. (1)

and Eq. (2), and illustrated in Fig. 4. The max operator in Eq. (1) shrinks the valleys in the spectra, while the min operator in Eq. (2) shrinks the peaks. Because of the differences in the shape and height of the peaks, the change of shrinking rate in the min operation in Eq. (2) is greater than that of the max operator in Eq. (1) after a certain scale ε. The changes in the upper profiles and lower profiles of a dense canopy vegetation spectrum are shown in Fig. 16 (for $\varepsilon = 6$–10) and Fig. 17 (for $\varepsilon = 26$–30). The changes in the upper profiles and lower profiles of a sparse canopy vegetation spectrum are shown in Fig. 18 (for $\varepsilon = 6$–10) and Fig. 19 (for $\varepsilon = 26$–30). It can be seen that the changes in the lower profiles for dense canopy vegetation and sparse canopy vegetation spectra are very similar for $\varepsilon = 6$–10, but quite different for $\varepsilon = 26$–30 (see the two circles in Figs. 17 and 19), as also shown in their fractal signature curves (Figs. 6–9).

As described in the methodology section, a unique list of scales were determined from the spectra of features at sample pixel locations, and fractal signatures were calculated at the scales that can be used to enhance the characteristics of the features. Therefore, the fractal signatures presented in this paper can be considered a multiscale feature-oriented approach to hyperspectral image processing. Although a single fractal signature image may not be able to distinguish between all features in the image, fractal signatures at multiple scales may provide additional information on the image features.

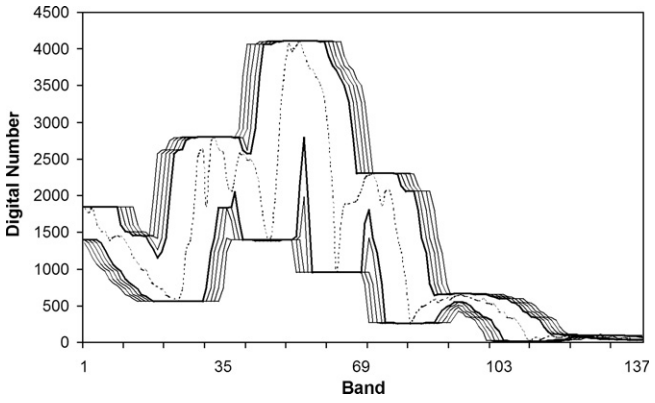

Fig. 16. Changes in the upper profiles and lower profiles of a dense canopy vegetation spectrum for $\varepsilon = 6$–10.

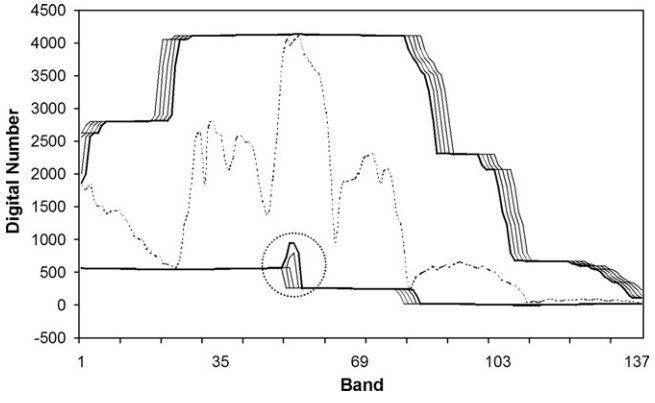

Fig. 17. Changes in the upper profiles and lower profiles of a dense canopy vegetation spectrum for $\varepsilon = 26$–30.

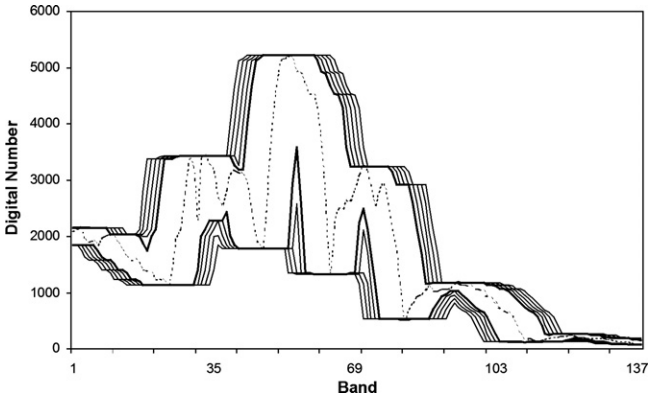

Fig. 18. Changes in the upper profiles and lower profiles of a sparse canopy vegetation spectrum for $\varepsilon = 6$–10.

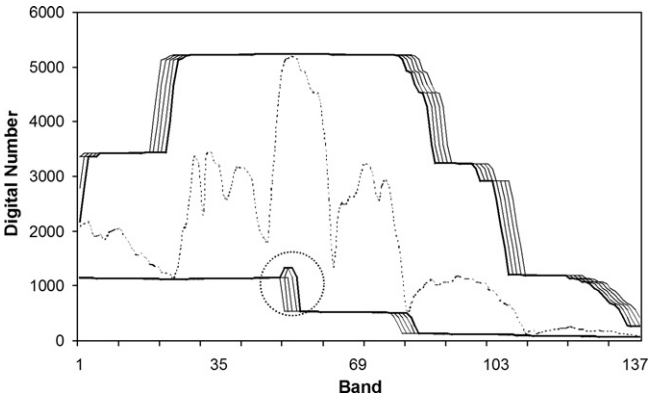

Fig. 19. Changes in the upper profiles and lower profiles of a sparse canopy vegetation spectrum for $\varepsilon = 26$–30.

5. Conclusions

Based on the fractal signature concept, a multiscale approach to hyperspectral image analysis was proposed and implemented in the Interactive Data Language (IDL). Using NASA's Earth Observing-1 (EO-1) Hyperion image from a study area in the Ray Roberts Greenbelt near Denton, Texas, USA, this paper demonstrated the capabilities of fractal signatures in discriminating different land cover types in three different ways: (1) fractal signature curves, (2) distances between fractal signatures, and (3) fractal signature images. The asymmetry in length measurement noticed by Mandelbrot (1967) has proven to be effective in handling hyperspectral curves obtained from Hyperion radiance data: measuring the lengths of spectral curves from above and from below at multiple scales can reveal important information on the features in the hyperspectral image. The contribution of fractal signature images has been shown through comparison of image classification results

for five land cover types: dense canopy vegetation, sparse canopy vegetation, soil, urban and water. The overall classification accuracy for the five land cover types was 64.07% using the maximum likelihood classification of six principal components (PC1, PC2, PC3, PC4, PC6, and PC7) derived from the 138-band Hyperion image. When four additional fractal signature images at certain scales were included for classification, the overall classification accuracy increased from 64.07% to 83.85%. Although detailed analysis and assessment of fractal signatures in hyperspectral image analysis is under way, the preliminary results from Hyperion radiance data suggest that fractal signatures at certain scales can reveal important differences in land cover types. Compared with fractal dimension which is limited to fractal objects, fractal signature works for both fractal and non-fractal objects. It would be interesting in future work to assess the use of fractal signatures for detecting subtle changes in reflectance spectra.

Acknowledgements

This research was supported by the University of North Texas (UNT) Faculty Research Grant G33657 and an Oak Ridge Associated Universities (ORAU) Ralph E. Powe Junior Faculty Enhancement Award. The sponsorships from UNT and ORAU are gratefully acknowledged. The author would like to thank two anonymous reviewers who provided helpful comments/suggestions.

References

Burrough, P.A. Fractal and Geochemistry, in: Avior, A. (Ed.), The Fractal Approach to Heterogeneous Chemistry. Wiley & Sons Ltd., pp. 383–405, 1989.

Clarke, K.C. Computation of the fractal dimension of topographic surfaces using the triangular prism surface area method. Computers and Geosciences 12, 713–722, 1986.

De Cola, L. Fractal analysis of a classified Landsat scene. Photogrammetric Engineering and Remote Sensing 55, 601–610, 1989.

De Jong, S.M., Burrough, P.A. A fractal approach to the classification of Mediterranean vegetation types in remotely sensed images. Photogrammetric Engineering and Remote Sensing 61, 1041–1053, 1995.

Dellepiane, S., Giusto, D.D., Serpico, S.B., et al. SAR image recognition by integration of intensity and textural information. International Journal of Remote Sensing 12, 1915–1932, 1991.

Devaney, R.L. Chaos, fractals, and dynamics – computer experiments in mathematics. Addison-Wesley Pub. Co., New York, 1990.

Dong, P. Lacunarity for spatial heterogeneity measurement in GIS. Geographic Information Sciences 6, 20–26, 2000a.

Dong, P. Test of a new lacunarity estimation method for image texture analysis. International Journal of Remote Sensing 21, 3369–3373, 2000b.

Hsu, P.-H., Tseng, Y.-H. Feature Extraction for Hyperspectral Image, in: Proceedings of the 20th Asian Conference on Remote Sensing, November 22–25 Hong Kong, China, vol. 1, pp. 405–410, 1999.

Hsu, P.-H., Tseng, Y.-H. Wavelet-based analysis of hyperspectral data for detecting spectral features, in: XIXth Congress of the International Society for Photogrammetry and Remote Sensing (ISPRS), July 16–23, Amsterdam, The Netherlands, TP VII-10-17/602, 2000.

Kaewpijit, S., Moigne, J.L., El-Ghazawi, T. Automatic reduction of hyperspectral imagery using wavelet spectral analysis. IEEE Transactions on Geoscience and Remote Sensing 41, 863–871, 2003.

Lam, N.S. Description and measurement of Landsat TM images using fractals. Photogrammetric Engineering and Remote Sensing 56, 187–195, 1990.

Landgrebe, D. On progress toward information extraction methods from hyperspectral data. Presented at the SPIE 42nd Annual Meeting, San Diego CA, July 27–August 1, 1997.

Lindeberg, T. Scale-space theory: a basic tool for analysing structures at different scales. Journal of Applied Statistics 21, 225–270, 1994a.

Lindeberg, T. Scale-Space Theory in Computer Vision. Kluwer Academic, Dordrecht, The Netherlands, 1994b.

Mandelbrot, B.B. How long is the coast of Great Britain: statistical self-similarity and fractional dimension. Science 155, 636–638, 1967.

Mandelbrot, B.B. Fractals, Forms, Chance and Dimension. Freeman, San Francisco, 1977.

Mandelbrot, B.B. The Fractal Geometry of Nature. Freeman, San Francisco, 1983.

Mathur, A., Bruce, L.M., Byrd, J. Discrimination of subtly different vegetation species via hyperspectral data, in: Proceedings of IEEE International Geoscience and Remote Sensing Symposium and the 24th Canadian Symposium on Remote Sensing, Toronto, Canada, June 24–28, vol. 2, pp. 805– 807, 2002.

Myint, S.W. Fractal approaches in texture analysis and classification of remotely sensed data: comparisons with spatial autocorrelation techniques and simple descriptive statistics. International Journal of Remote Sensing 24, 1925–1947, 2003.

NASA, 2002. Hyperion: <http://eo1.gsfc.nasa.gov/miscPages/Results/Sec_02.pdf/>.

Pearlman, J.S., Barry, P.S., Segal, C.C., et al. Hyperion, a Space-Based Imaging Spectrometer. IEEE Transactions on Geoscience and Remote Sensing 41, 1160–1172, 2003.

Peleg, S., Noar, J., Hartley, R., et al. Multiple resolution texture analysis and classification. IEEE Transactions on Pattern Analysis and Machine Intelligence, PAMI-6, 518–523, 1984.

Pentland, A. Fractal-based description of natural scenes. IEEE Transactions on Pattern Analysis and Machine Intelligence, PAMI-6, 661–674, 1984.

Pu, R., Gong, P. Wavelet transform applied to EO-1 hyperspectral data for forest LAI and crown closure mapping. Remote Sensing of Environment 91, 212–224, 2004.

Qiu, H.-L., Lam, N.S., Quattrochi, D.A., et al. Fractal characterization of hyperspectral imagery. Photogrammetric Engineering and Remote Sensing 65, 63–71, 1999.

Rees, W.G. Measurement of the fractal dimension of ice-sheet surfaces using Landsat data. International Journal of Remote Sensing 13, 663–671, 1992.

Roach, D., Fung, K.B. Fractal-based textural descriptors for remotely sensed forestry data. Canadian Journal of Remote Sensing 20, 59–70, 1994.

Schowengerdt, R.A. Remote Sensing: Models and Methods for Image Processing, third ed Academic Press, New York, 2006.

Tsai, F., Philpot, W. Derivative analysis of hyperspectral data. Remote Sensing of Environment 66, 41–51, 1998.

Ungar, S.G., Pearlman, J.S., Mendenhall, J.A., et al. Overview of the Earth Observing One (EO-1) Mission. IEEE Transactions on Geoscience and Remote Sensing 41, 1149–1159, 2003.